Electronic Supplementary Information

Ag_2Se/conjugated polyelectrolyte heterojunction films for high-performance flexible thermoelectrics

Yu-Chi Peng[a], Chih-Wei Hsu[a], Haim Kwon[b], Po-Shen Lin[a], Moon Sung Kang[c], Han Young Woo[b], and Cheng-Liang Liu[a,d,e,*]

[a] Department of Materials Science and Engineering, National Taiwan University, Taipei 10617, Taiwan

[b] Department of Chemistry, Korea University, Seoul 02841, Republic of Korea

[c] Department of Chemical and Biomolecular Engineering, Sogang University, Seoul 04107, Republic of Korea

[d] Institute of Polymer Science and Engineering, National Taiwan University, Taipei 10617, Taiwan

[e] Advanced Research Center for Green Materials Science and Technology, National Taiwan University, Taipei 10617, Taiwan

Characterization

The measurements were conducted under a helium atmosphere. Ultraviolet-visible-near-infrared (UV-vis-NIR) spectra were recorded on a Hitachi U-4100 spectrophotometer with a resolution of 1 cm^{-1}. The structural confirmation was carried out using X-ray diffraction (XRD) on a Rigaku Ultima IV powder diffractometer with CuKα radiation (λ = 0.15406 nm). Fourier transform infrared spectroscopy (FTIR) were acquired using a Perkin Elmer L160000F. X-ray photoelectron spectroscopy (XPS) was performed using a PHI 5000 VersaProbe III system (ULVAC-PHI, Inc.) under ultra-high vacuum conditions (6.7×10^{-8} Pa), with a monochromatic Al Ka(1.4keV) and Cr Ka(5.4keV) as the excitation beam. The morphology of the composite films observed using field emission scanning electron microscopy (FE-SEM) were acquired using JEOL JSM-7600F. Transmission electron microscopy (TEM) analysis was performed on a JEOL JEM-2100F were utilized to observe the surface morphology and microstructure of the composite films. Energy dispersive spectrometer (EDS) elemental mapping images were performed using an OXFORD X-Max (SEM-EDS) and OXFORD X-MaxN TSR (TEM-EDS). Hall effect measurements were performed using an M91 FastHall™ system (Lake Shore Cryotronics, Inc.), with the final values averaged over 500 individual measurements. The in-plane Seebeck coefficient (S) and electrical conductivity (σ) of the nanocomposite samples were measured using a commercially available thermoelectric tester ZEM-3 (Advance Riko). Photoelectron spectroscopy in air (PESA) spectra was measured by Riken Keiki Surface Analyzer (Model AC-2S Pro Alpha DC). Thermogravimetric analysis (TGA) and differential scanning calorimetry (DSC) profiles were derived by using Discovery TGA 55 thermogravimetry, Netzsch 209 F3/ Bruker Tensor II and DSC25 (TA instrument) respectively.

Table S1. Comparison of room-temperature thermoelectric characteristics of Ag_2Se-based composite films reported in the literature and in this work.

Material	*S* [μV K^{-1}]	*σ* [S cm^{-1}]	*PF* [μW m^{-1} K^{-2}]	Ref.
PI/Ag_2Se[b]	-134.1	1440	2590	[1]
Nylon/PVP:Ag_2Se[a]	-143.4	929	1910	[2]
PEDOT:Ag_2Se: CuAgSe[a]	-121.8	1080	1603	[3]
Ag_2Se:PPy[a]	-144	1064	2240	[4]
PEI:Ag2Se[a]	-137.1	1190.76	2239	[5]
Ag_2Se:PEDOT: PSS[a]	-155.3	859.6	2074	[6]
Nylon/Ag_2Se[b]	-143.0	919.8	1882	[7]
Ag_2Se	-121	1060	1526.4	[8]
Nylon/Ag_2Se[b]	-140.7	497	987.4	[9]
Ag:Ag_2Se[a]	-67.5	3598	1860.6	[10]
BC:Ag_2Se[a]	-167	230	642	[11]
Ag:Ag_2Se[a]	-89.6	3030	2436	[12]
SWCNTs:Ag_2Se[a]	-108.1	1656.64	1936	[13]
Ag_2Se/CPE[a]	-104.0	2209.7	2629.2	This work

[a] ":" represents material mixing in a bulk heterojunction (BHJ).

[b] "/" represents a layered planar heterojunction (PHJ).

Table S2. Comparison of XPS Binding Energies for Ag_2Se and BHJ film.

Element	Binding Energy [eV] (Ag_2Se)	Binding Energy [eV] (BHJ)
Ag 3d	373.9	372.6
	368	366.6
Se 3d	54.4	54.3
	53.5	52.5
S 2p	167.2	167.5
	165.9	166.2
	163.4	163.7
	162.1	162.3

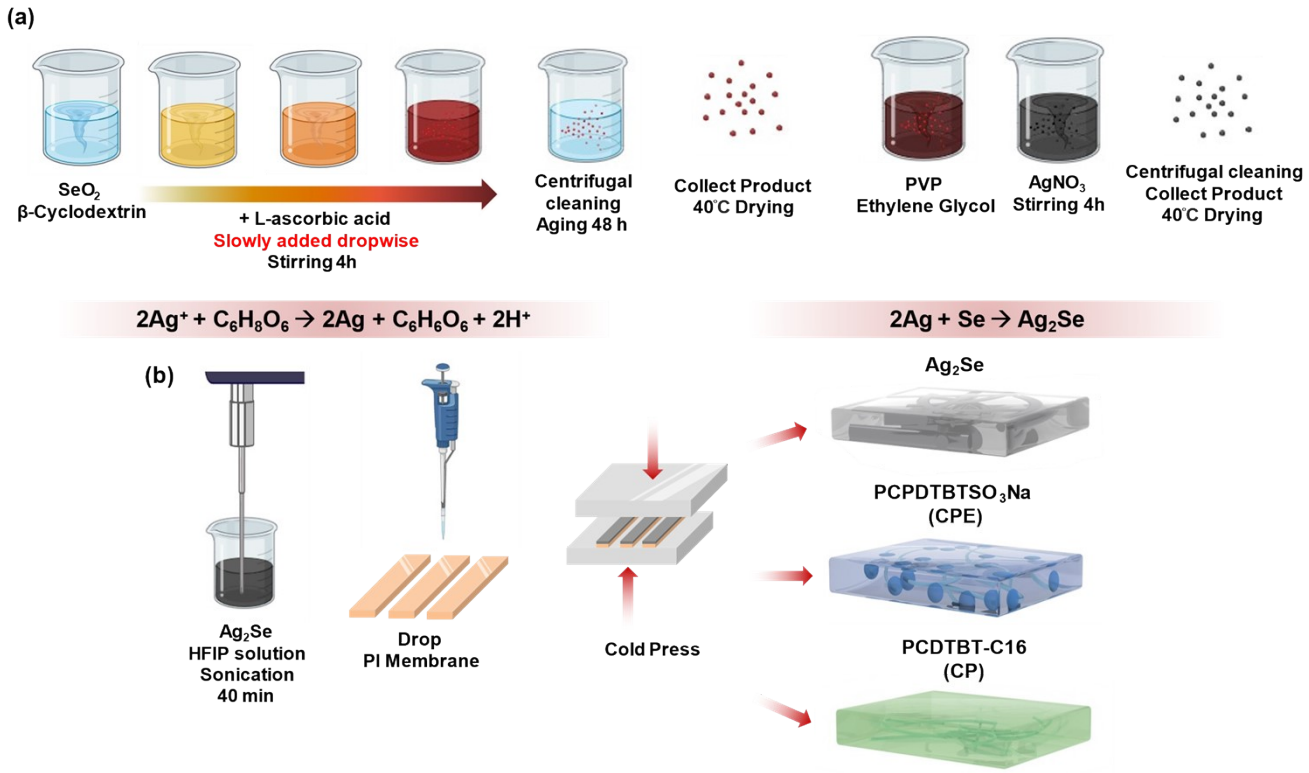

Figure S1. Schematic illustration of the fabrication processes for (a) Ag_2Se and (b) Ag_2Se-based composite films with different heterojunction architectures.

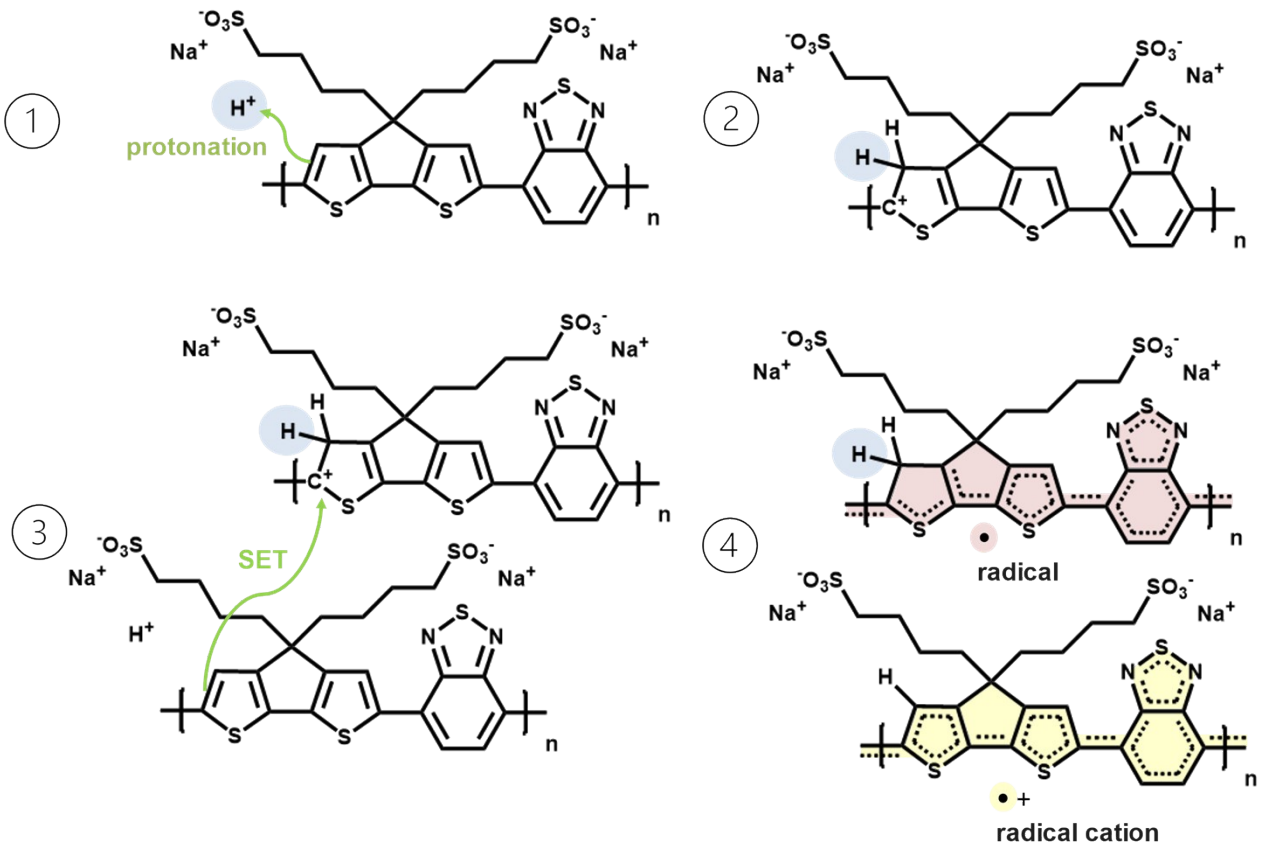

Figure S2. Schematic illustration of the protonic acid doping process of CPE, showing the proposed transient intermediates and the single-electron-transfer (SET) mechanism leading to the formation of the final self-doped species.

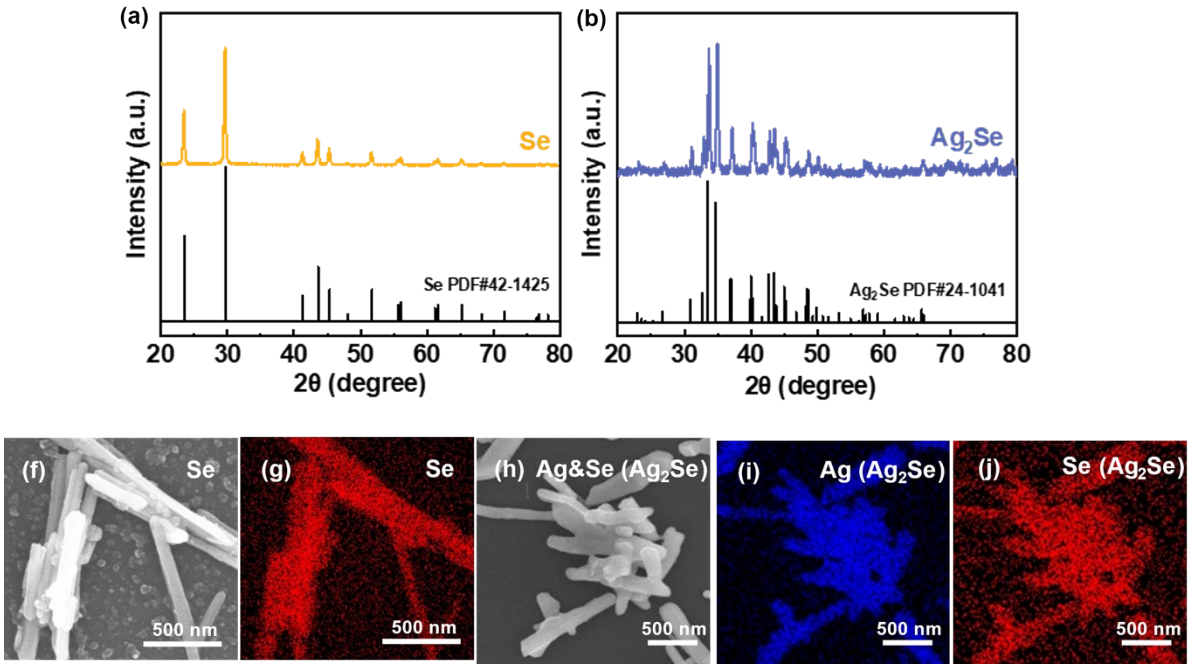

Figure S3. (a, b) X-ray diffraction (XRD) patterns of Se and Ag_2Se nanowire. The SEM images of (c, e) Se nanowire and Ag_2Se nanowire. EDS elemental mapping images show the spatial distributions of (d) Se and (f, g) Ag and Se of Ag_2Se.

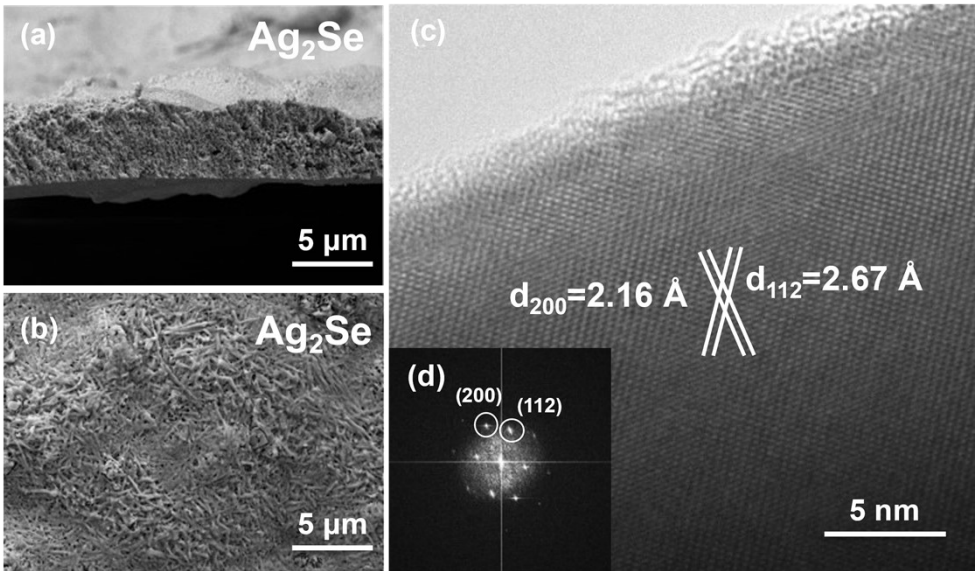

Figure S4. (a, b) Top-view and cross-sectional SEM images of the Ag_2Se film. (c, d) TEM image with the corresponding fast Fourier transform (FFT) pattern shown in the lower-left inset. (e-g) Transmission electron microscopy (TEM) analyses of the BHJ film: (e) TEM image with the corresponding fast Fourier transform (FFT) pattern shown in the lower-left inset. (f) BHJ film overlaid with EDS elemental mapping; and (g) showing the spatial distributions of Ag and S within the film.

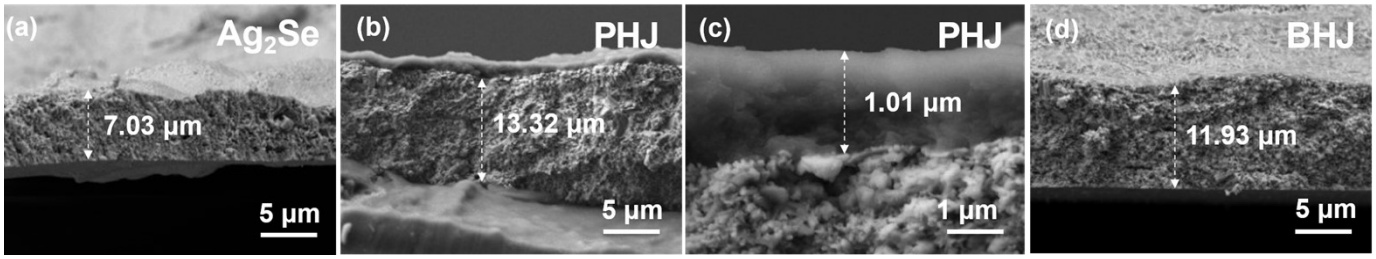

Figure S5. Cross-sectional SEM images used to determine film thickness, measured using the built-in SEM analysis software. (a) Ag_2Se film. (b, c) PHJ film at magnifications of 3 k× and 20 k×, respectively; (c) highlights the enlarged view of the CPE top layer. (d) BHJ film.

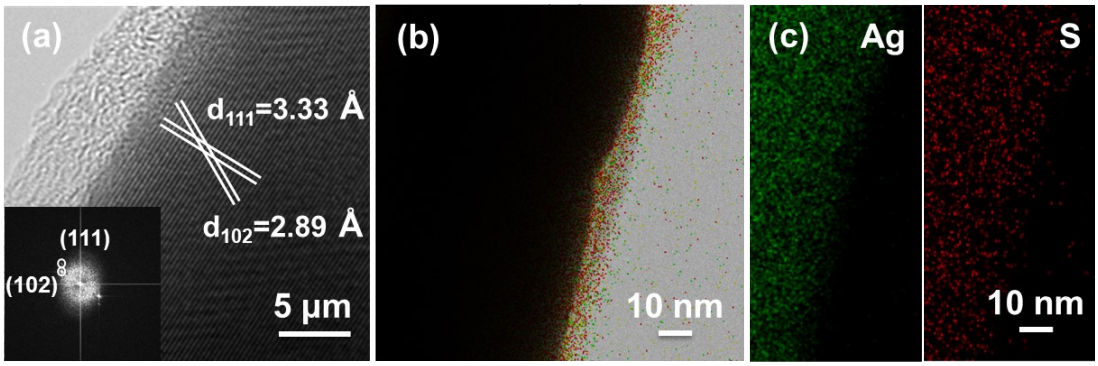

Figure S6. (a-c) Transmission electron microscopy (TEM) analyses of the BHJ film: (a) TEM image with the corresponding fast Fourier transform (FFT) pattern shown in the lower-left inset. (b) BHJ film overlaid with EDS elemental mapping; and (c) showing the spatial distributions of Ag and S within the film.

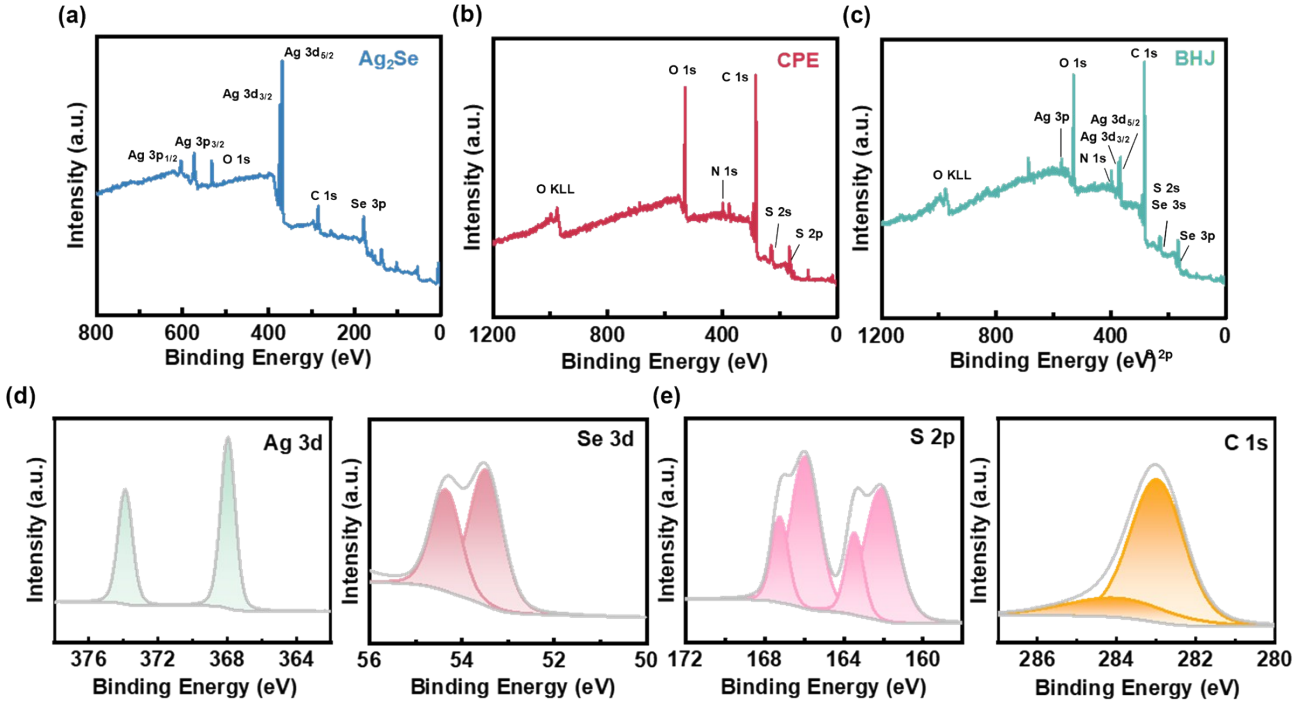

Figure S7. X-ray photoelectron spectroscopy (XPS) spectra of (a) Ag_2Se, (b) CPE and (c) BHJ films. High-resolution XPS spectra of (d) Ag_2Se and (e) CPE.

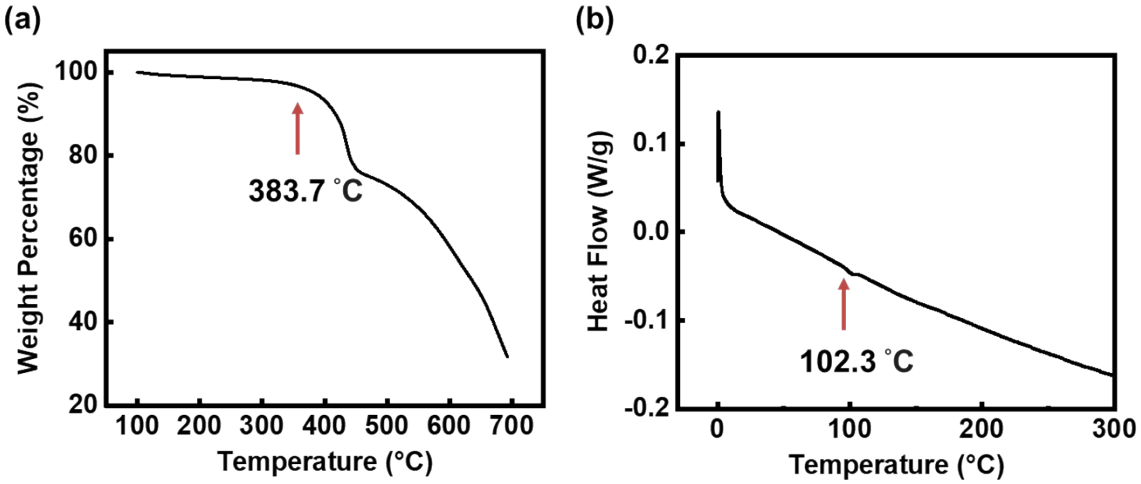

Figure S8. (a) Thermogravimetric analysis (TGA) and (b) differential scanning calorimetry (DSC) curves of the polymer CPE.

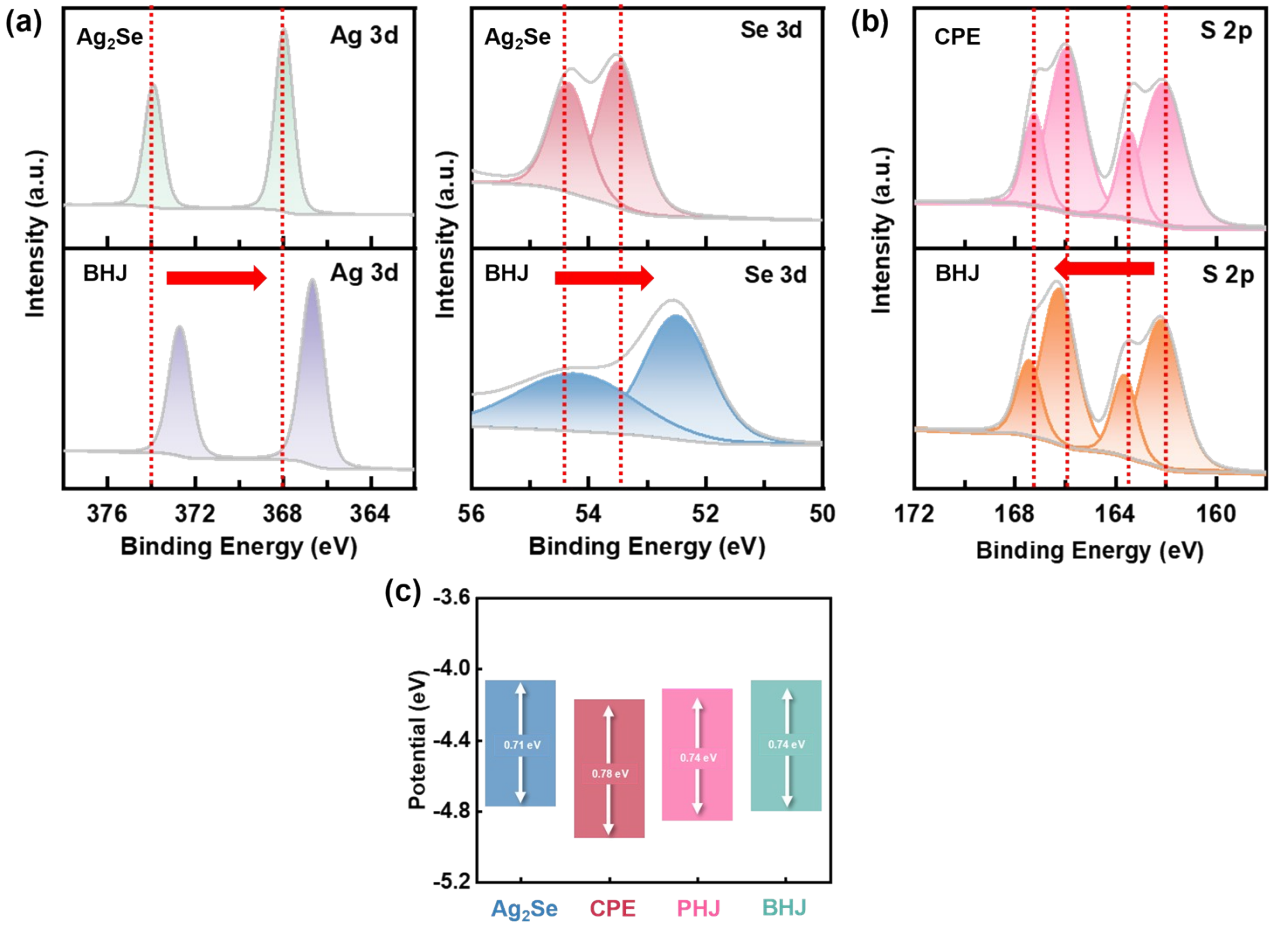

Figure S9. High-resolution X-ray photoelectron spectroscopy (XPS) spectra of (a) Ag_2Se and BHJ films (b) CPE and BHJ films. (c) The band gap distribution of the Ag_2Se, CPE, PHJ and BHJ.

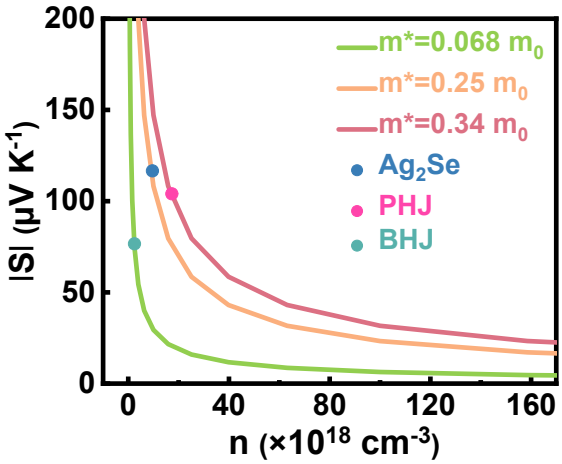

Figure S10. n-dependent |S| calculated by the single-parabolic-band (SPB) model and the measured values in experiments included for comparison.

The synergistic effect of the planar heterojunction is further elucidated through Single Parabolic Band (SPB) analysis. Pristine Ag_2Se is characterized by an effective mass of approximately 0.25 m_0, whereas the PHJ configuration exhibits an apparent increase to ~0.34 m_0. This shift suggests that the ordered interfacial architecture not only enhances carrier concentration, as reflected by the increased n, but also modifies the density-of-states effective mass at the Ag_2Se /CPE interface. The concurrent increase in carrier density and effective mass mitigates the conventional trade-off between electrical conductivity and Seebeck coefficient, thereby contributing to the enhanced power factor observed in the PHJ system. In contrast, the BHJ structure exhibits a reduced carrier concentration accompanied by an apparent effective mass approaching 0.068 m_0. This behavior implies that the random mixing does not sustain the interfacial modulation effect. Instead, structural disorder and heterogeneous phase distribution likely introduce additional carrier scattering, causing the transport properties to revert toward a lower effective-mass regime. These results collectively indicate that an ordered planar architecture plays a critical role in preserving interfacial electronic modulation and optimizing charge transport in organic–inorganic thermoelectric hybrids.

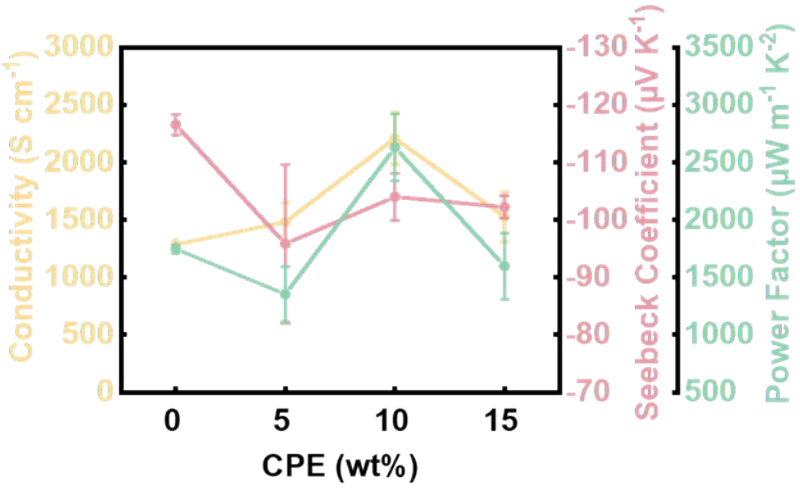

Figure. S11. The thermoelectric performance of CPE ratio onto the Ag_2Se film.

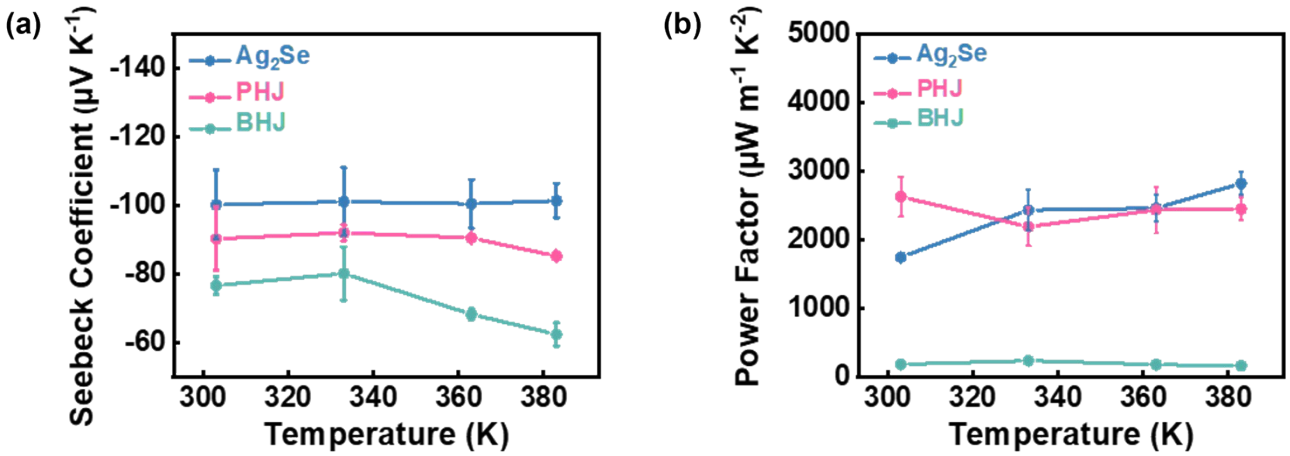

Figure S12. Temperature-dependent (a) Seebeck coefficient and (b) power factor of Ag_2Se and composite films (PHJ, BHJ).

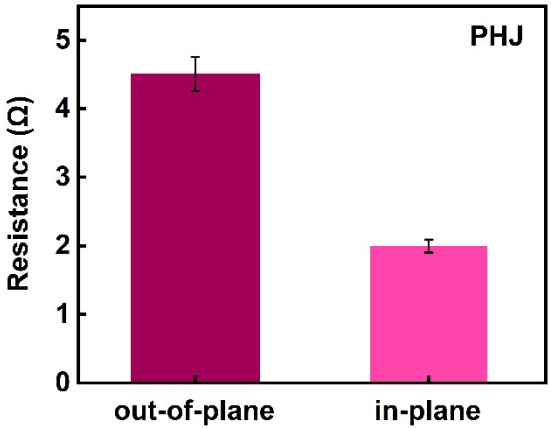

Figure S13. The resistance of the in-plane and out-of-plane measurement setup for PHJ film.

Table S3. Comparison of TEG power generation performance with reported literature.

Material	*ΔT* [K]	*output voltage* [mV]	Ref.
Ag_2Se:Ag:PEDOT	27	5.6	[14]
Ag_2Se	30	13.43	[15]
Ag:Ag_2Se	29.6	16.1	[12]
Se:Ag_2Se	30	14.9	[16]
Ag2Se/CPE	29.6	14	This work

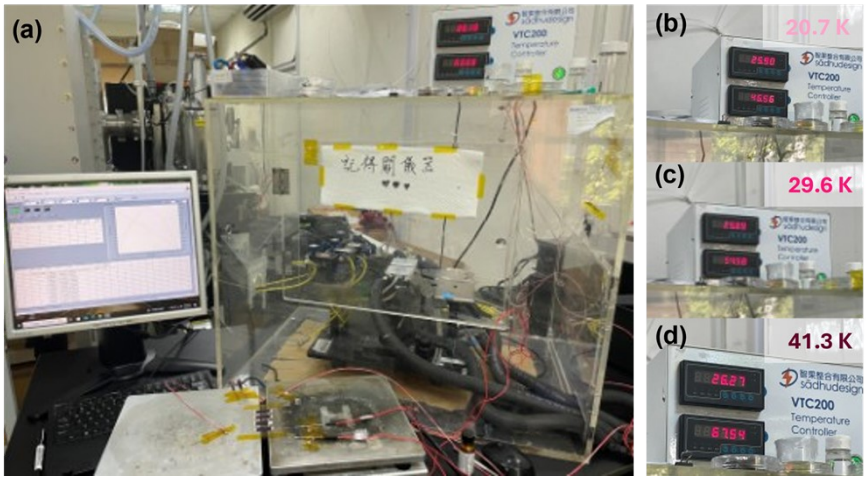

Figure S15. (a) Testing photographs of flexible thermoelectric generator (TEG), and the different temperature gradient actual situation at (b) 20.7 K, (c) 29.6 K, (d) 41.3 K.

Reference

1. Y. Lei, R. Qi, M. Chen, H. Chen, C. Xing, F. Sui, L. Gu, W. He, Y. Zhang, T. Baba, T. Baba, H. Lin, T. Mori, K. Koumoto, Y. Lin and Z. Zheng, *Adv. Mater.*, 2022, **34**, 2104786.
2. C. Jiang, P. Wei, Y. Ding, K. Cai, L. Tong, Q. Gao, Y. Lu, W. Zhao and S. Chen, *Nano Energy*, 2021, **80**, 105488.
3. Y. Lu, Y. Qiu, K. Cai, X. Li, M. Gao, C. Jiang and J. He, *Mater. Today Phys.*, 2020, **14**, 100223.
4. Y. Li, Q. Lou, J. Yang, K. Cai, Y. Liu, Y. Lu, Y. Qiu, Y. Lu, Z. Wang, M. Wu, J. He and S. Shen, *Adv. Funct. Mater.*, 2022, **32**, 2106902.
5. Q.-X. Hu, W.-D. Liu, L. Zhang, H. Gao, D.-Z. Wang, T. Wu, X.-L. Shi, M. Li, Q.-F. Liu, Y.-L. Yang and Z.-G. Chen, *Adv. Energy Mater.*, 2024, **14**, 2401890.
6. R. Wang, R. Sun, Y. Ren, Y. Ma and L. Ma, *J. Mater. Sci. Mater. Eng.*, 2025, **20**, 31.
7. C. Jiang, Y. Ding, K. Cai, L. Tong, Y. Lu, W. Zhao and P. Wei, *ACS Appl. Mater. Interfaces*, 2020, **12**, 9646–9655.
8. D. Lee, W. Park, Y. A. Kang, H. T. Lim, S. Park, Y. Mun, J. Kim and K.-S. Jang, *ACS Appl. Mater. Interfaces*, 2023, **15**, 3047–3053.
9. Y. Ding, Y. Qiu, K. Cai, Q. Yao, S. Chen, L. Chen and J. He, *Nat. Commun.*, 2019, **10**, 841.
10. Q. Gao, W. Wang, Y. Lu, K. Cai, Y. Li, Z. Wang, M. Wu, C. Huang and J. He, *ACS Appl. Mater. Interfaces*, 2021, **13**, 14327–14333.
11. D. Palaporn, W. Mongkolthanaruk, K. Faungnawakij, K. Kurosaki and S. Pinitsoontorn, *ACS Appl. Energy Mater.*, 2022, **5**, 3489–3501.
12. X. Li, Y. Lu, K. Cai, M. Gao, Y. Li, Z. Wang, M. Wu, P. Wei, W. Zhao, Y. Du and S. Shen, *Chem. Eng. J.*, 2022, **434**, 134739.
13. Q.-X. Hu, W.-D. Liu, L. Zhang, W. Sun, H. Gao, X.-L. Shi, Y.-L. Yang, Q. Liu and Z.-G. Chen, *Chem. Eng. J.*, 2023, **457**, 141024.
14. Z. Wang, Q. Gao, W. Wang, Y. Lu, K. Cai, Y. Li, M. Wu and J. He, *Mater. Today Phys.*, 2021, 21, 100553.
15. L. Zhang, G. Song, D. Luo, Y. Chen, Y. Wu and J. You, *Mater. Sci. Eng. B*, 2025, **320**, 118445.
16. Y. Liu, Y. Li, M. Wu, Y. Lu, Z. Wang, P. Wei, W. Zhao and K. Cai, *ACS Appl. Mater. Interfaces*, 2023, **15**, 36587–36593.